

Redshifting and Broadening of Quantum-Well Infrared Photodetector's Response via Impurity-Free Vacancy Disordering

Deepak Sengupta, Vikram Jandhyala, Sangsig Kim, Weich Fang, Jay Malin, Peter Apostolakis, Kwong-Chi Hseih, Yia-Chung Chang, Shun Lien Chuang, Sumith Bandara, Sarath Gunapala, Milton Feng, Eric Michielssen, and Greg Stillman

Abstract—The partial intermixing of the well and barrier materials offers unique opportunities to shift locally the bandgap of quantum-well (QW) structures. We have demonstrated redshifting and broadening of the wavelength responses of bound-to-continuum GaAs and InP based quantum-well infrared photodetectors (QWIP's) after growth via impurity-free vacancy disordering (IFVD). A comprehensive set of experiments is conducted on QWIP's fabricated from both as-grown and multiple-quantum-well (MQW) structures. Compared to the as-grown detector, the peak spectral responses of the disordered detectors were shifted to longer wavelengths. The peak absolute response of the disordered GaAs based QWIP is lower by almost a factor of four. However, the responsivity characteristics of the disordered InP based QWIP show no major degradation. In general, with the spectral broadening taken into account, the overall performance of the disordered QWIP's has not dropped significantly. Thus, the postgrowth control of the QW composition profiles by impurity-free vacancy disordering offers unique opportunities to fine tune various aspects of a photodetector's response. Theoretical calculations of the absorption coefficient spectrum are in excellent agreement with the experimental data.

Index Terms—Absolute response, dark current characteristics, focal plane array, impurity-free vacancy disordering, peak response wavelength, quantum efficiency, quantum-well infrared photodetectors, rapid thermal annealing, red shift.

I. INTRODUCTION

DETECTING, measuring, and imaging the patterns of thermal heat radiation emitted by objects have been of interest since the discovery of the infrared (IR) spectrum

Manuscript received March 23, 1998; revised July 7, 1998. This work was supported by the NASA Office for Space Science and by the Microelectronics Laboratory, University of Illinois at Urbana-Champaign, Urbana, IL 61801 USA. The work of D. Sengupta was supported under a fellowship by the National Academy of Sciences-National Research Council. The work of V. Jandhyala and E. Michielssen was supported by the Air Force Office of Scientific Research via the Multi University Research Initiative Program under Contract F49620-96-1-0025. This work was performed by the Center for Space Microelectronics Technology, Jet Propulsion Laboratory, California Institute of Technology, Pasadena, CA 91109 USA.

D. Sengupta, S. Bandara, and S. Gunapala are with Jet Propulsion Laboratory, California Institute of Technology, Pasadena, CA 91109 USA.

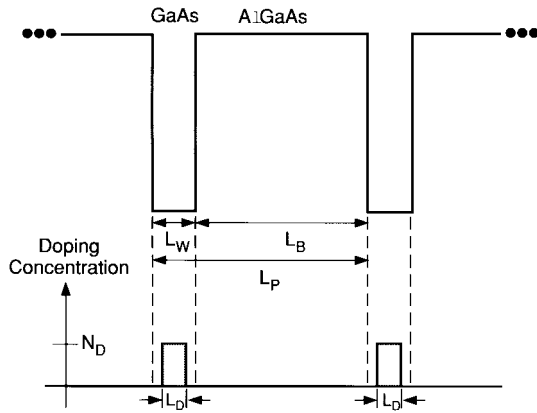
V. Jandhyala is with Ansoft Corporation, Pittsburgh, PA 15219 USA.

S. Kim, W. Fang, J. Malin, P. Apostolakis, K.-C. Hseih, S. L. Chuang, M. Feng, E. Michielssen, and G. Stillman are with Department of Electrical and Computer Engineering, University of Illinois at Urbana-Champaign, Urbana, IL 61801 USA.

Y.-C. Chang is with Department of Physics, University of Illinois at Urbana-Champaign, Urbana, IL 61801 USA.

Publisher Item Identifier S 1077-260X(98)06934-2.

in 1800 by astronomer Herschel [1]. IR sensors have been extensively developed since the 1940's. The first practical IR detector was PbS [2]. This polycrystalline thin-film photoconductor operates via a band-to-band transition in the 1–3- μm range [3]. Lead salt detectors, such as PbS and PbSe, are chemically deposited, and operate at any temperature between 300 K and 77 K [2]. These detectors have found use in medical instruments, exhaust gas analyzers, fire control, and power meters [4]. Intrinsic semiconductor detectors such as Ge:Hg or Si: x are minority carrier devices, which rely on the photo excitation of impurity levels within the bandgap of the host material [2]. In use, the devices are cooled until only a few of the hydrogenic impurities are thermally ionized. The principal problems with the devices are their low operating temperatures (~ 24 K), and low impurity absorption coefficient, which is limited by low-impurity solubility. To achieve total absorption in Si: x , the detectors would require a thickness of 100 μm [3]. Until the development of mercury cadmium telluride (MCT) detectors, the detector of choice for the 8–12- μm -long wavelength infrared (LWIR) band was Ge:Hg photoconductor. The HgCdTe (MCT) detector was introduced in the late 1950's in England [2]. These detectors have found use in both civilian and military applications in thermal imaging, guidance, reconnaissance, ranging, and communication systems [1]. The versatility comes from the ability to grow custom alloy mixtures of $\text{Hg}_{1-x}\text{Cd}_x\text{Te}$ with virtually any bandgap between 1–25 μm [2]. The MCT detector has several advantages over the extrinsic photoconductor. The band-to-band absorption coefficient of MCT is much greater than the impurity absorption of intrinsic semiconductors, thus permitting the construction of thinner detectors with larger quantum efficiencies. The MCT can also operate at a higher temperature than Ge:Hg, since the intrinsic detectors must be cooled to very low temperatures to detect impurity transitions over thermal noise. From the standpoint of device-to-device uniformity, MCT cannot replace Ge:Hg [3]. Whereas conventional IR imaging is performed using bandgap transition in MCT p-n diodes, IR imaging can also be performed using the intersubband transition in a multiquantum-well (MQW) III–V semiconductor structure. The concept of using the intersubband absorption of IR radiation in a QW structure as a photoconductive device was proposed in 1980 by Esaki, Sai-Halasz, and Chang [4]. The first experimental study in the



- L_W = Well width (40Å)
- L_B = Barrier width (300Å)
- L_P = Width of one period of the structure (340Å)
- L_D = Width of intentionally doped region in the quantum well (center 20Å of quantum well)
- N_D = Doping concentration intentionally introduced in the quantum well over a region of width L_D ($1.0 \times 10^{18}/\text{cm}^3$)

Fig. 1. Schematic drawing of the type-I QW structure. The parameters for the standard structure are indicated above.

literature was performed by Smith and co-workers in 1983 [5]–[7].

II. N-TYPE QWIP DESIGN AND DEVELOPMENTS

Modern photoconductive quantum-well infrared photodetectors (QWIP's), with responses at various wavelengths from 5 to 12 μm , were first demonstrated by Levine *et al.* in 1987 [8]. A schematic of the type-I QWIP structure is shown in Fig. 1. In most QWIP devices, a signal is generated when a QW absorbs IR radiation. This excites electrons from the ground state to an excited state from which the excited electron is collected by an applied field, resulting in photocurrent. Superlattice detectors are, therefore, extremely versatile due to the nearly limitless possibilities of bandgap engineering (three fundamental structures: bound-to-bound, bound-to-continuum, and bound-to-miniband). Besides the successful GaAs–AlGaAs superlattice, other III–V materials have indicated promise as LWIR detectors. In recent years, considerable interest has focused on the fabrication and characterization of III–V based QWIP [9]. The use of these materials rather than conventional mercury cadmium telluride detector is based upon two advantages: First, these detectors are fabricated from GaAs–Al_xGa_{1-x}As QW superlattices, a significantly less expensive, more uniformly grown, and more abundant material than MCT. Second, standard high-yield GaAs integrated circuit fabrication techniques may be used, paving the way for advanced sensor arrays and their cost effective manufacture with existing infrastructure. The price paid for the easy fabrication of QWIP's is in their lower quantum efficiency and higher dark current than ideal narrow gap detectors such as HgCdTe [10]. The many fabrication problems in MCT make it generally unsuitable for a large array technology

TABLE I
COST COMPARISON BETWEEN HgCdTe FPA AND QWIP FPA

10 μm Detector	HgCdTe FPA	QWIP FPA
Material cost	\$3000/inch ²	\$300/inch ²
Size of Wafer	7 inch ²	7 inch ²
Lot Cost (10 wafers, 2 inch dia)	\$210,000	\$21,000
Processing Cost (for 70 inch ²)	\$140,000	\$20,000
Total Cost	\$350,000	\$41,000
Chip Yield (FPA)	25%	50%
Chip Cost Reduction	17	1

or monolithic integration. Here is where QWIP's find their niche. The GaAs–AlGaAs QWIP is easier to fabricate, less expensive to grow, and more uniform across large-area two-dimensional (2-D) focal plane arrays (FPA's) at a lower cost. Long-wavelength imaging systems such as: 15 μm cutoff 128 \times 128 QWIP FPA Camera, 256 \times 256 Portable QWIP FPA Camera, 9- μm cutoff 640 \times 486 QWIP FPA Camera, and 256 \times 256 Palm-size QWIP Camera utilizing intersubband transition in III–V QW's have been demonstrated by the Jet Propulsion Laboratory [11] and achieved an excellent imagery with a noise equivalent differential temperature of 30 mK. Incremental engineering advancements are quickly changing the perspective on QWIP, toward one of great hope, as the successor to MCT in LWIR array technology. Cost issues affect the development and future commercialization of such a technology. The focal plane array (FPA) chip cost reduction will be at least 17 to 1 using the QWIP approach as illustrated in Table I.

The QWIP detector uses a QW energy transition to absorb optical radiation and the accompanying excited state electron for signal output [12]. In a bound-to-continuum type (schematically shown in Fig. 1) QWIP detection, a single bound state contributes its photoexcited electron to the extended state in the continuum, above the barrier, where the electron is collected by applying an electric field across the superlattice [13]. Unexcited or bound state electrons cannot easily tunnel through the thick barriers, hence dark current is relatively low [13]. The disadvantage of this QW system is that it cannot absorb normally incident light, due to polarization selection rules [14]. Grating couplers are important components of QWIP focal plane imaging arrays. Gratings provide a means to scatter the optical field in directions that favor intersubband absorption [15]. Recent discussion in the literature has provided several solutions to the coupling problem [16].

A recently developed fast electromagnetic solution technique, the steepest descent fast multiple method (SDFMM) [17], permits the efficient analysis of scattering from periodic and aperiodic gratings [18]. In the context of QWIP gratings, the SDFMM can be used to predict absorption as a function of wavelength, as shown in Fig. 2. The P-grating [Fig. 2(a)] is a doubly periodic grating; D- and S-gratings [Fig. 2(b) and (c)] are perturbed P-gratings, obtained by respectively displacing and scaling raised portions of the periodic grating in the lateral directions in a random manner. As seen in Fig.

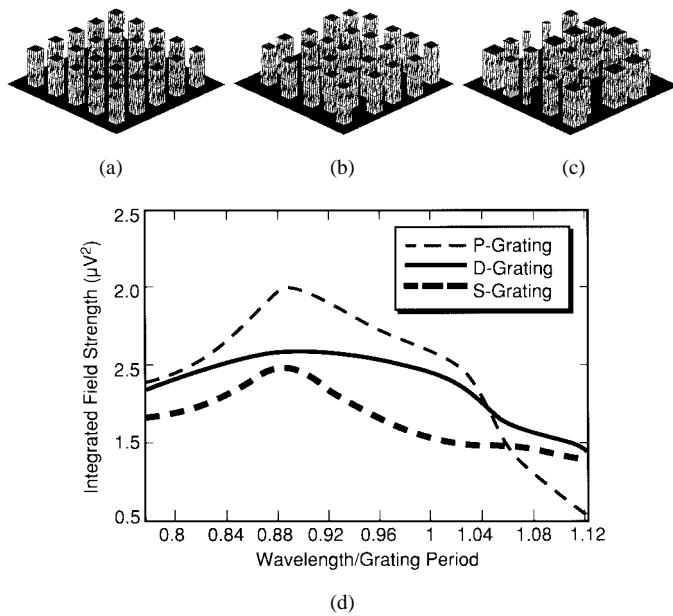


Fig. 2. Integrated field strength versus wavelength/period for P-, D-, and S-gratings. Optical current on these gratings is modeled using 30 000 basis functions (a) P-grating, (b) D-grating, (c) S-grating.

2(d), the D- and S-gratings exhibit a much smoother spectral behavior over the wavelength range of interest than the P-grating, albeit with a slightly reduced peak absorption. Rough surface gratings [Fig. 3(a)], which are logical extensions of quasirandom gratings, are within the range of applicability of the SDFMM. The (rough) surfaces modeled in the paper can be created using techniques developed for fabricating diffractive optical elements [19]. Fig. 3(b) shows the spectral response of the integrated field strength due to rough gratings. The absorption remains high and has a remarkably constant behavior over the entire wavelength band of interest. These observations suggest that adding randomness to gratings, for instance by introducing rough surfaces, can result in a dramatic amelioration in peak absorption and spectral behavior with a resulting improvement in QWIP performance.

QWIP's have recently been explored in great detail with promising results. The largest drawback is their large dark currents when operated above 60 K. A number of different methods have been explored in an effort to reduce this current. IR hot electron transistors [20] utilizing a GaAs-AlGaAs MQW structure as an emitter and an electron energy filter in front of the collector as shown in Fig. 4(a) and (b) are designed for higher performance at 60 K and above. The energy filter is designed to selectively filter the photocurrent and the dark current respectively. Draining the dark current allows the QWIP to operate at higher temperatures with reduced noise. The injection coefficient ($\Delta I_C / \Delta I_E$) of the photoelectron measured as the ratio of the relative changes in the photocurrent are shown in Fig. 5(a) and (b), respectively.

Measurements were done for the two cases of bias at different heat sink temperatures. In general, a high-injection coefficient results. Also, another figure-of-merit estimating the reduction in the leakage current relative to reduction in photocurrent are also shown in Fig. 5(a) and (b), respectively.

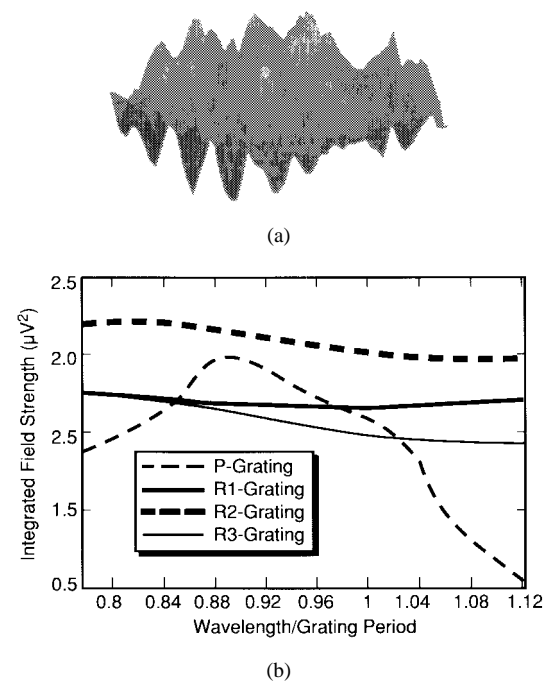


Fig. 3. Integrated field strength versus wavelength/period for rough surface gratings and a periodic grating. The three gratings R1, R2, and R3 possess root mean square heights of 0.2, 0.4, and 0.6 times the center wavelength respectively. For these gratings, their correlation length is varied analogously to the period. (a) R-grating. (b) Spectral Behavior of Absorption.

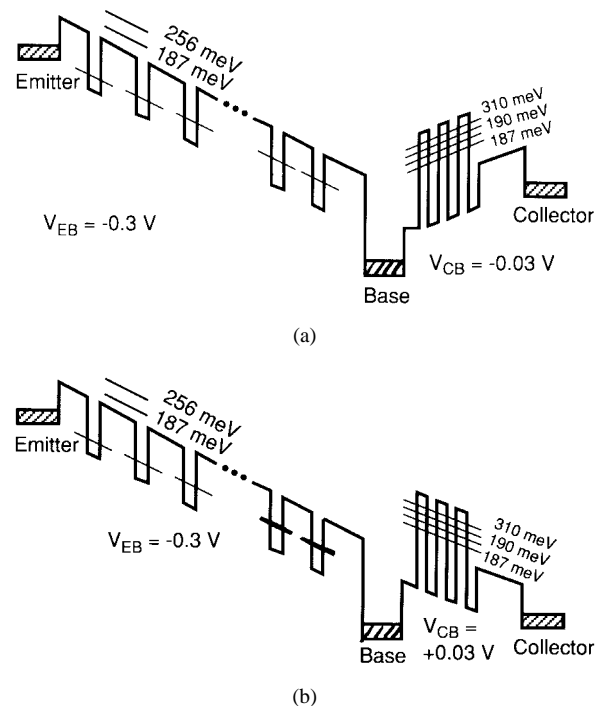


Fig. 4. Band edge profile of an IR hot electron transistor utilizing a multiple QWIP with an energy filter barrier (a) $V_{EB} = -0.3$ V and $V_{CB} = 0.03$ V, (b) $V_{EB} = -0.3$ V and $V_{CB} = -0.03$ V.

In spite of the successful development of intersubband MQW QWIP technology, only little effort has focused on broad spectrum/multiple color detection [21], [22]. One of the distinct advantages of the QW approach is the ability to

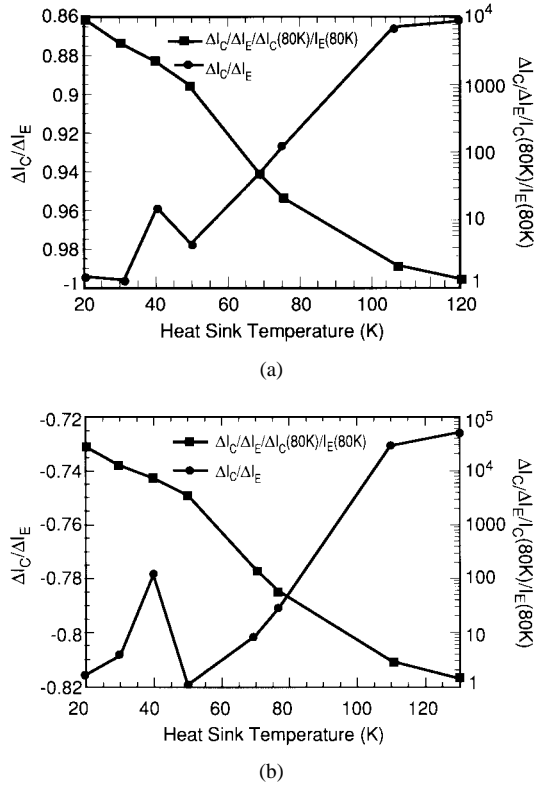


Fig. 5. Injection coefficient of the photoelectron ($\Delta I_C/\Delta I_E$) of a QWIP with energy filter. (a) $V_{EB} = -0.3$ V, $V_{CB} = 0.03$ V. (b) $V_{EB} = -0.3$ V and $V_{CB} = -0.03$ V. Also shown $((\Delta I_C/\Delta I_E)/(I_C(80\text{ K})/I_E(80\text{ K})))$ estimating the reduction in the leakage current relative to the reduction in the photocurrent.

produce multiband or multicolor detectors, which are desirable for future high-performance IR systems. Interdiffusion offers the flexibility to modify the properties of the materials after growth and can be achieved by techniques, such as impurity-induced disordering, impurity-free vacancy disordering [23], [24], or ion implantation enhanced interdiffusion [25], [26]. It is possible to disorder the QW's such that the bound state energy is blue shifted, leading to a corresponding red shift of the intersubband energy. The QW is changed from a square well with a sharp interface, to an error-function shaped well with a corresponding change in the confined energy levels [27]–[29]. The degree to which disordering occurs depends not only on the processing, but on the physical properties of the material, including, but not limited to, dielectric encapsulant type, doping, and the existence of capping layers.

In this paper, we describe experimental results for detectors in which impurity free vacancy disordering is employed to intermix GaAs–AlGaAs and InGaAs–InP MQW structures. We first present the details of our experiments and measurement procedures. Then, the experimental results for both as-grown and disordered structures are compared and discussed. Next, a brief discussion of our theoretical calculations of the intersubband absorption coefficient for as-grown and disordered GaAs–AlGaAs QWIP's are described, and the prediction of the model is compared to the experimental data. Finally, we conclude with a summary of the relative performances of as-grown and disordered QWIP.

III. LAYER DISORDERING BY RAPID THERMAL ANNEALING

Modifying the layer (i.e., QW and/or barrier width) thickness will change the absorption wavelength of the raw material. In this manner, one can grow detectors which are tuned for absorption at various wavelengths. This method, however, relies on a separately grown superlattice, possibly on different substrates for each different absorption peak wavelength desired. An alternate method to achieving variation in absorption peaks which can easily be employed is the technique known as impurity-free vacancy disordering accomplished by the diffusion of point defects such as the column III (Ga) vacancies [27], [28]. Thus, by disordering the well using the native point defects which exist within the well and vacancies introduced at the surface, it is possible to increase the first energy state in the conduction band, such that a reduction in energy to the continuum is achieved. This allows for a red shift in the intersubband energy without growing an entirely new structure. The redistributed profile makes the QW thinner at the bottom than the originally grown well, as shown in Fig. 6(a). This modification of the well width shifts the absorption to longer wavelengths as the energy level rises in the well. Dielectric film stress, transferred to the surface of the substrate, influences the amount of diffusion induced wavelength shifting which will occur during annealing. Deposition may take place via chemical vapor deposition (CVD), plasma-enhanced chemical vapor deposition (PECVD), or sputtering. Substrate temperature, reactant gas composition, and for PECVD, microwave power applied to the plasma will change the film characteristics. Films such as silicon dioxide and silicon nitride, with their myriad of compositions and mixtures should be adequate to provide arbitrary variety in stress levels. The annealing operation may be performed via rapid thermal annealing (RTA). In recent years, laser irradiation to induce QW intermixing in GaAs–AlGaAs and GaInAs–GaInAsP structures has been demonstrated [30]–[33]. Laser beam sources as processing tools allows thermal processing of semiconductors with very high spatial and temporal resolution [34], [35]. Hence, the use of this technique offers unique opportunities to fine tune various aspects of a QWIP's response. Once the annealing is complete, the dielectric cap layer may be stripped and the wafers prepared for subsequent detector processing. Broad-spectrum/multicolor detection makes use of the variation in wavelength shift for different dielectric induced surface stress. Fig 6(b)–(d) illustrates that the broad spectrum response is a direct result of the linear super position of two adjacent absorption maxima.

IV. GROWTH, MATERIAL, AND DEVICE CHARACTERIZATION

GaAs–AlGaAs n-type QWIP's were grown by solid source molecular beam epitaxy (MBE) on a semi-insulating (001) GaAs substrate. The active region, sandwiched between two n-type (10^{18} cm $^{-3}$) GaAs layers, consisting of 50 periods of 300-Å undoped Al $_{0.25}$ Ga $_{0.75}$ As barriers and 40-Å Si ($n \sim 10^{18}$ cm $^{-3}$) center doped GaAs wells. The doping is confined to the center 20 Å of the GaAs well. InGaAs–InP p-type QWIP's consisted of 30 periods of 10-Å uniformly doped

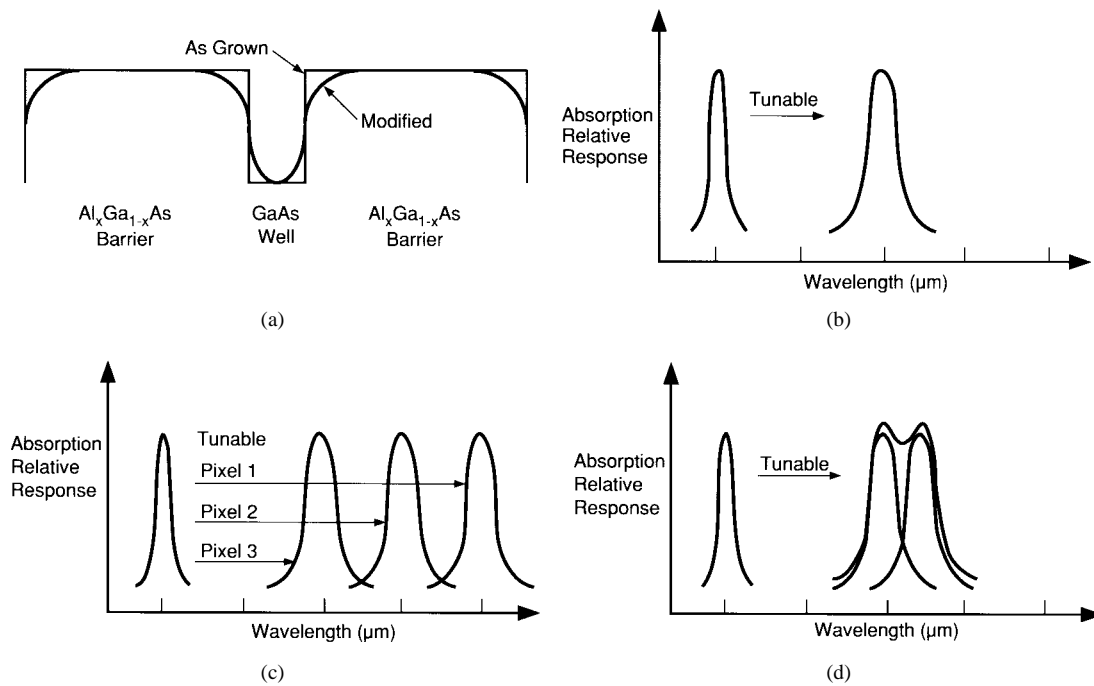


Fig. 6. (a) Modification of QW profile due to QW-intermixing. (b) Schematic representation of shifting effect and its utility for response detector tuning. (c) Multicolor detection by shifting each pixel a different amount. (d) Schematic representation of a broadband detector made possible through the linear superposition of the relative absorption response of two neighboring peaks.

($p = 3 \times 10^{18} \text{ cm}^{-3}$) $\text{In}_{0.53}\text{Ga}_{0.47}\text{As}$ QW's and 500 Å thick, uniformly Be-doped ($p = 1 \times 10^{17} \text{ cm}^{-3}$) InP barriers, all of which were sandwiched between 500 Å Be-doped ($3 \times 10^{18} \text{ cm}^{-3}$) $\text{In}_{0.53}\text{Ga}_{0.47}\text{As}$ contacts on an InP substrate. DCXRD measurements were carried out to characterize the crystalline quality of the p-type InGaAs-InP superlattice layer (SL). A Phillips double-crystal X-ray diffractometer was used to measure the diffraction patterns. Each of the diffraction patterns were measured in a mode with a fine collimation of the incident and diffracted X-rays in order to retrack the evolution of its superlattice harmonics over several degrees. Fig 7(a) shows the experimental and simulated (004) $\text{CuK}\alpha_1$, rocking curves of the p-QWIP structure with 30 periods of InGaAs/InP SL (10Å InGaAs well and 500-Å InP barriers). The superlattice satellites are observed up to the fourth order, and the average FWHM of the experimental satellite peaks is 31 arc-sec, demonstrating excellent material quality. The simulation in Fig 7(b) assumed abrupt interfaces for both InGaAs-on-InP and InP-on-InGaAs interfaces, and that in Fig. 7(c) assumes a monolayer of $\text{InAs}_{0.5}\text{P}_{0.5}$ inserted at the upper interfaces of the InGaAs layer. Clearly, a transitional monolayer in the group V sublattice gives a much better agreement than the abrupt interface does between experiment and simulation, suggesting residual As_2 incorporation in the InP layers and formation of strained monolayers at the interfaces. In this case, a period consists of three layers: 10.5-Å $\text{In}_{0.475}\text{Ga}_{0.525}\text{As}$, 3.04 Å $\text{InAs}_{0.5}\text{P}_{0.5}$ and 5.643Å InP and to atomic layer schematic can be expressed as In-P-In-P*-GaIn-As-GaIn-As*-In*AsP*-In-P-In-P.

In all studies, prior to annealing, the samples were first degreased in trichloromethane, acetone, and methanol followed by a light surface etch using NH_4OH . Then, a 1200-Å

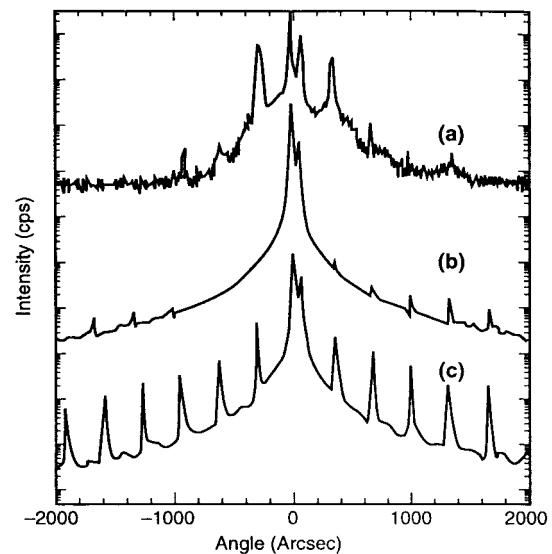


Fig. 7. High resolution double-crystal X-ray diffraction rocking curves of a 30-period InGaAs-InP QWIP structure. (a) Experimental rocking curves of the p-type QWIP structure. (b) Simulation assuming abrupt interface for both InGaAs-on-InP and InP-on-InGaAs interfaces. (c) Simulation assuming a monolayer of $\text{In}_{0.5}\text{As}_{0.5}\text{P}$ inserted at each inverted interface.

SiO_2 encapsulant is deposited by plasma enhanced chemical vapor deposition. Rapid thermal annealing was performed in an AET RTA reactor with 10 sccm of N_2 flowing. The temperature was stabilized at 200 °C prior to high temperature anneal which consists of ramping the temperature at a rate of 60 °C/s until an anneal temperature (850° and 950 °C for the GaAs-AlGaAs samples and 700, 800, and 900 °C for the InGaAs-InP) is reached. The temperature is maintained at the anneal temperature for 30 s, after which a cool down

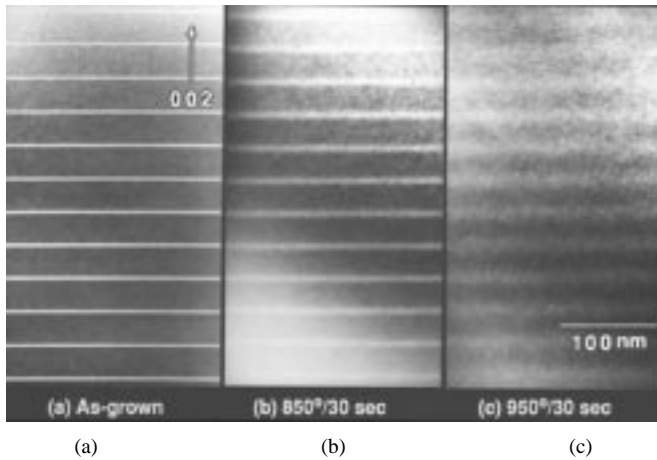


Fig. 8. Cross-sectional TEM of the (a) as-grown (b) disordered (850 °C, 30 s), and (c) RTA (950 °C, 30 s) n-type GaAs–AlGaAs MQW structures. Shown are the QW's (lighter regions) and the barriers (darker regions).

is initiated and the temperature decreases to 600 °C after 10 s and to 250 °C after 1 min.

The material quality and optical properties of the as-grown and disordered GaAs–AlGaAs and InGaAs–InP MQW samples were investigated using cross-sectional TEM, PL, and IR absorption measurements. TEM was performed with a 120-KV Philips CM12 microscope. In its PL measurements, the MQW samples are cooled to 77 K and excited with the 632.8-nm line of an He–Ne laser. Their luminescence is analyzed by a 0.5-m SPEX monochromator and detected with a liquid-nitrogen cooled Ge detector. The intersubband absorption is measured at room temperature using a Bomem DA3 FTIR spectrophotometer. The MQW samples were polished into multipass waveguides and sandwiched between two IR-transmitting KRS-5 slabs. IR measurements were done using a glowbar source and a KBr beam splitter. Detection of the IR beams was achieved using a 77-K photoconductive HgCdTe (MCT) detector.

The cross-sectional TEM micrographs are shown in Fig. 8 for (a) an as-grown MQW and (b) disordered GaAs–AlGaAs MQW annealed at 850 °C for 30 s. No defects or dislocations were observed, and the QW's (light regions) were measured to be ~ 45 Å and the barriers (dark region) ~ 300 Å. A shift widening of the well width was observed in the 850 °C case. The cross-sectional TEM micrographs are shown in Fig. 9 for (a) an as-grown InGaAs/InP MQW and (b) disordered MQW annealed at 800 °C for 30 s. No defects or dislocations were observed for both as-grown and disordered MQW regions.

In Fig. 10, the 77-K PL spectrum shows a blue shift of $0.03 \mu\text{m}$ (65.0 meV) for the disordered QWIP structure in comparison to the as-grown structure. In addition, the broad disordered QWIP structure exhibits a reduction in luminescence intensity. This is attributed to the out-diffusion of Si dopant atoms from the well and is strongly dependent on the amount of disordering during the anneal. Fig. 11 illustrates the 6 K PL spectra of the samples capped with SiO₂ and followed by RTA at temperatures 700, 800, 900 °C for 30 s. The dependent of the blue shift in PL peak emission energies on temperatures was observed (~ 24.0 meV @ 700 °C, ~ 132.2

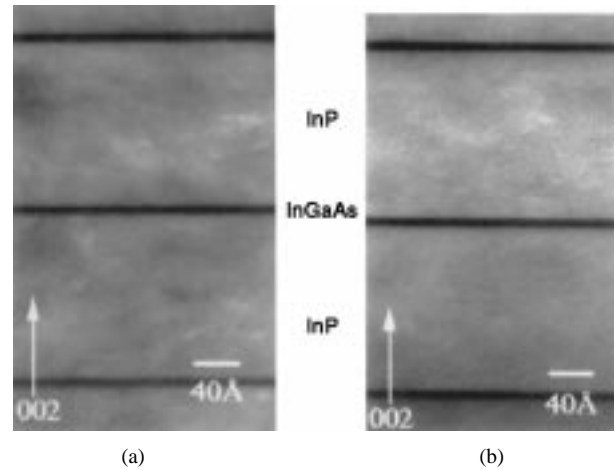


Fig. 9. Cross-sectional TEM of the (a) as-grown, and (b) disordered (800 °C for 30 s) ultra-thin p-type InGaAs–InP MQW structures. Shown are the QW's (darker regions) and the barriers (lighter regions).

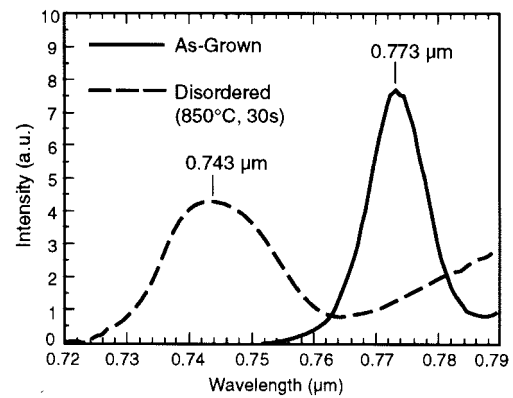


Fig. 10. PL spectra at 77 K of the (a) as-grown and (b) disordered (850 °C, 30 s) n-type GaAs–AlGaAs MQW structure. A blue shift of 65 meV is observed.

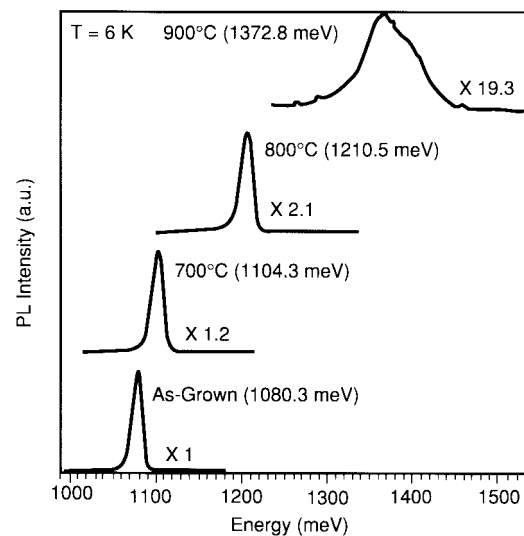


Fig. 11. PL spectra at 6 K of the as-grown and disordered (700, 800, and 900 °C for 30 s) ultra-thin p-type InGaAs–InP MQW structures.

meV @ 800 °C, and ~ 292.5 meV @ 900 °C). In addition, Fig. 12 shows no significant degradation of the PL linewidth up to

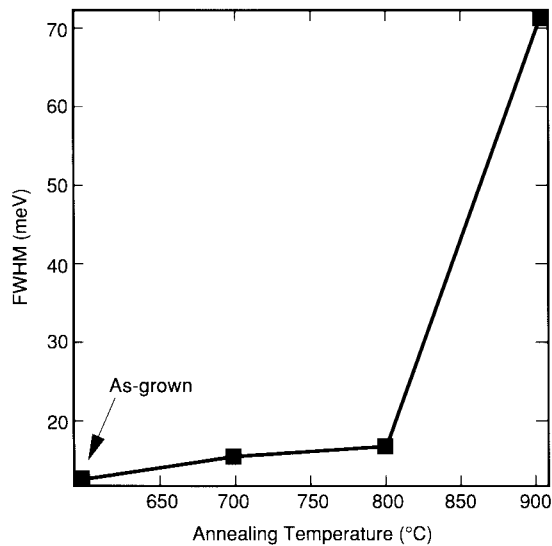


Fig. 12. 6-K PL linewidth of the as-grown and disordered (700, 800, and 900 °C for 30 s) ultra-thin p-type InGaAs-InP MQW structures.

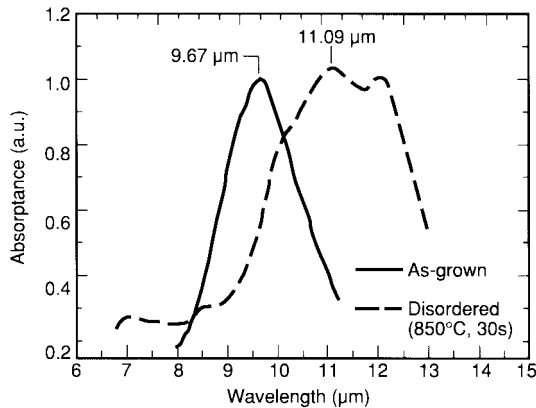


Fig. 13. Room-temperature absorption spectrum of the (a) as-grown and (b) disordered (850 °C, 30 s) n-type GaAs-AlGaAs MQW structure. A red shift of 16 meV is observed.

800 °C RTA. Beyond 800 °C RTA, disordered QWIP structure also exhibits a reduction in peak luminescence intensity, which may be due to the overall broadening of the peak response as well as any defects that the annealing process might have introduced.

The room-temperature intersubband absorption measurements are shown in Fig. 13. The measurements were made at room temperatures in the standard waveguide geometry (45° edge coupling). The absorption of the buffer layer and substrate were subtracted in order to isolate the absorption of the QW structure. The broad intersubband absorption is due to the continuum band above the energy barriers. The absorption peak for the as-grown QWIP structure is measured to be 9.67 μm (128 meV), while its disordered QWIP shows a broader response with the absorption peak at 11.09 μm (12 meV), resulting in a red shift of 1.42 μm (16 meV). The shift of the absorption resonance in n-doped GaAs-AlGaAs QW's is due to both the interdiffusion-induced modification of the confining potential and the decrease in the polarization shift [27]. Shifting and broadening of the intersubband absorption

peak was observed. The broadened spectral response of the structure is due to the nonuniform disordering within the MQW structure. Each well in the broad spectrum structure has a slightly different potential profile and yields a slightly different spectral response. Therefore, the total spectral response, which is a summation of spectral responses from each well, should be both broader and smaller in magnitude.

We also note that the magnitude of the energy shift of the intersubband transition in the conduction band is not in agreement with the interband energy shift, which should obey the 67/33 conduction band to valence band offset ratio for the AlGaAs-GaAs material system. This is due to the nature of the PL measurement and depth dependence of the layer disordering during rapid thermal annealing. Since the pump light from the He-Ne laser is strongly absorbed by GaAs, only the wells near the top of the MQW stack can be probed and measured for luminescence. Since these top wells have a larger amount of disordering and intermixing than the average well in the stack, the measured PL wavelength for the RTA MQW sample shows a much larger blue shift than expected.

QWIP's were fabricated from the as-grown and broad spectrum samples into 200-μm circular mesas by etching through the upper contact layers and the MQW structures down to the bottom contact layer. Ohmic contacts to the n-doped contact layers are subsequently formed by evaporating and alloying AuGe-Ni-Au (n-type GaAs-AlGaAs) or Ti-Au (p-type InGaAs-InP) metallization. All dark current, spectral response, and noise measurements on these as-grown and broad spectrum QWIP's were performed with the detectors mounted on a stage which is in thermal contact with the cold end of a continuous flow helium cryostat. The cryostat has an IR transmitting KRS-5 window which gives the detectors a 60° field-of-view for a 300 K background. The dark current ($I-V$) characteristics of the QWIP were measured with an HP 4145 semiconductor parameter analyzer at various temperatures. In order to obtain the absolute spectral response of the as-grown and broad spectrum QWIP's, both blackbody and relative spectral response measurements were performed. The detector were electrically connected to an external bias circuit, and bias currents were supplied from a battery in series with a large resistor which maintains a constant bias current. The temperature-dependent dark current versus voltage ($I-V$) characteristics of the fabricated as-grown and broad spectrum QWIP's are shown in Fig. 14. The dark current characteristics for the as-grown detectors are in agreement with what is reported by several authors [9]. At low temperatures and low biases, sequential tunneling through the barriers is dominant. At very low temperatures and intermediate bias, the as-grown detector exhibits a plateau in the dark current. At high temperatures and low biases, the dark current is dominated by thermionic emission of carriers from the wells and thermally assisted tunneling through the barriers. Fowler-Normham tunneling is the dominant mechanism with impact ionization reported at very high biases.

At each temperature, the dark current of the broad spectrum QWIP was higher than that of the as-grown detector, which will affect the noise performance of the broad spectrum QWIP. At low temperatures, both the as-grown and the broad

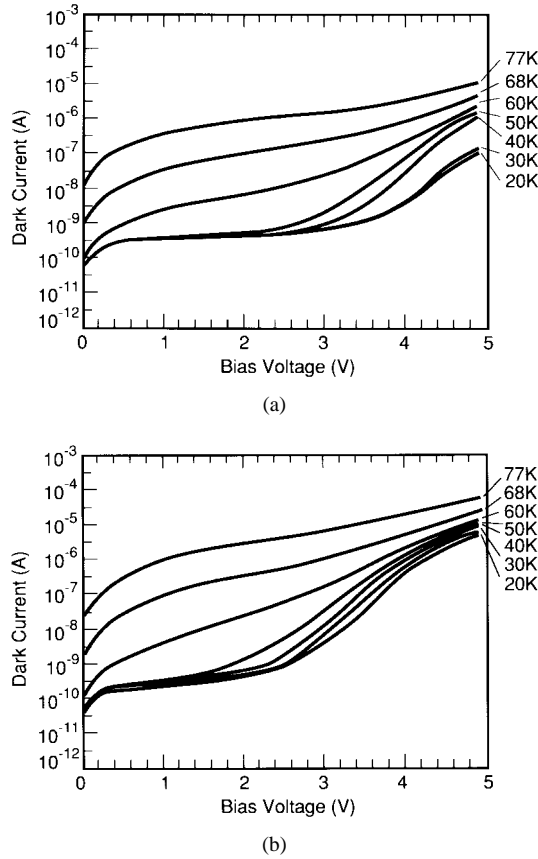


Fig. 14. Dark current versus bias characteristics as a function of temperature for the (a) as-grown (b) disordered (850 °C, 30 s) n-type GaAs–AlGaAs QWIP with cold shielding.

spectrum detectors exhibit a rapid increase in dark current at high biases. The onset for rapid increase occurs at a lower bias in the broad spectrum detector than in the as-grown detector. At higher temperatures, both the as-grown and the disordered detectors show a steady increase in the dark current as a function of applied bias. The larger dark current of the broad spectrum detector relative to the as-grown detector can be understood by examining the effects of interdiffusion on the energy subbands in a multiple-quantum structure. As shown schematically in Fig. 15(a) for zero applied bias, and in Fig. 15(b) for applied bias, the ground state energy (E_1) of an annealed MQW structure is higher than (E_1^0) of an as-grown structure due to increased aluminum mole fraction inside the well which results from layer intermixing during annealing. At a given applied bias, the dark current is proportional to the product of the energy dependent transmission coefficient through the barrier and the Fermi–Dirac distribution integrated over energy from ground state to infinity.

The rounded condition band edge profile of the disordered MQW structure results in a higher tunneling probability for electrons due to a larger transmission coefficient and lower barrier height. Consequently, at higher temperatures, where thermionic emission and thermally assisted tunneling dominate, the dark current of the disordered detector is higher than that of the as-grown detector. At low temperatures and low-to-moderate applied biases, the major contribution to the dark current results from electron tunneling through its barrier. In

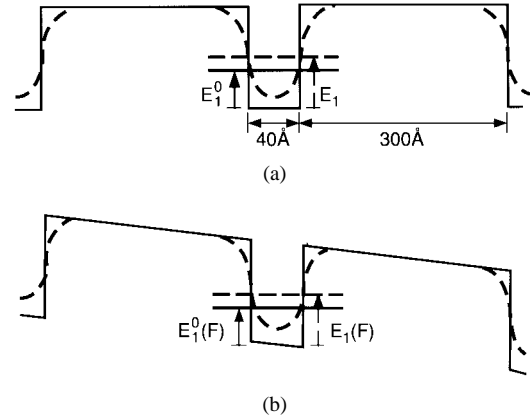


Fig. 15. A schematic diagram of an AlGaAs–GaAs superlattice before (solid line) and after (dashed line) rapid thermal annealing with (a) zero applied bias and (b) applied bias. E_1^0 and E_1 represent the zero bias ground state eigenvalue of the as-grown and the RTA structure, respectively. $E_1^0(F)$ and $E_1(F)$ represent the ground state eigenvalues under applied bias. Note the difference in the effective barrier height of the two profiles for nonzero biases.

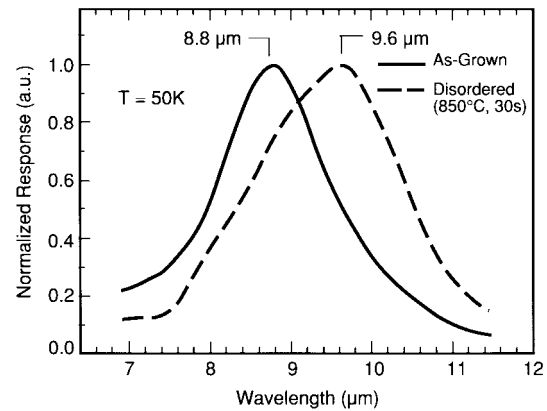


Fig. 16. Normalized photoresponse, of the as-grown (solid line) and the disordered @ 850 °C for 30 s (dotted line) n-type GaAs–AlGaAs QWIP at $T = 50$ K. The response is measured for each QWIP biased to operate at its peak performance.

this case, the dark current of the disordered structure lies at higher energy than the as-grown detector, and transmission of electrons through the barrier is larger due to a lower effective barrier height. This lower effective barrier height of the disordered detector may also explain the lower onset voltage for the rapid increase in the dark current in the disordered QWIP.

The spectral response and noise of the as-grown and broad spectrum QWIP's were measured with each detector biased to operate at their peak blackbody response. In Fig. 16 we show the normalized photoresponse for both the as-grown and disordered detectors. The photoresponse data are based on 45° edge coupling. The peak response wavelength measured are 8.8 μm for the as-grown detector and 9.6 μm for the disordered detector. Since the ground state (E_1) is higher and the effective barrier height is lower in the broad spectrum QWIP than in the as-grown QWIP, the peak response wavelength of the disordered QWIP experiences a long wavelength shift [27], in agreement with the room temperature intersubband absorption measurement.

From the blackbody and relative spectral response measurements, the peak absolute responses are calculated using (1) to be 0.37 A/W for the as-grown detector and 0.1557 A/W for the disordered detector. The total absorbed optical intensity is determined by integrating over wavelength the product of the normalized spectral response $r(\lambda)$ and the blackbody irradiance spectrum $W(\lambda, T)$. The peak absolute response R_p (A/W) is calculated from the absorbed optical intensity and the peak blackbody photocurrent I_p as

$$R_p = \frac{I_p}{M_F \frac{a^2}{a^2 + d^2} A t \cos \theta \int W(\lambda, T) r(\lambda) d\lambda} \quad (1)$$

where M_F is the modulation factor of the chopped blackbody source, a is the aperture radius, d is the distance between the blackbody and QWIP, A is the QWIP area, t is the transmission through the KRS-5 window, T is the blackbody temperature, and θ is the angle (45°) of incident radiation. The peak responsivity of the disordered QWIP is reduced to nearly a factor of four from the as-grown structure. The unity gain quantum efficiency is calculated from the absolute response using (2). Once the peak absolute response is determined, the unity gain quantum efficiency can be calculated using

$$\eta = \frac{R_p}{\lambda_p} \left(\frac{hc}{q} \right) \quad (2)$$

where R_p is the peak absolute response and λ_p is the peak wavelength of the spectral response. The peak quantum efficiencies are 8.11% for the as-grown and 2% for the broad spectrum GaAs–AlGaAs detector. The four times reduction in quantum efficiency in the broad spectrum QWIP is due primarily to the degraded peak responsivity and secondarily its red shift in the peak region wavelength. Also, the decrease in the response for the disordered QWIP could be attributed due to the decrease in gain by scattering. Although the broadened absorption spectrum of the SiO₂ encapsulated disordered detector can result in a reduced spectral response, we believe that the dominant reduction is a consequence of the out-diffusion of Si dopant from the well [28] and the increased dark current throughout the disordered MQW structure. The out-diffusion of Si atoms from the well reduced the surface concentration of electrons in the ground state and yields a smaller absorption coefficient. Using (3), the detectivity D^* for a peak wavelength of 8.8 μm , a chopping frequency of 500 Hz and a noise bandwidth of 1 Hz is calculated to be $1.445 \times 10^{10} \text{ cm} \cdot \sqrt{\text{Hz}}/\text{W}$ for the as-grown detector and $0.287 \times 10^{10} \text{ cm} \cdot \sqrt{\text{Hz}}/\text{W}$ at a peak wavelength of 9.6 μm for the disordered detector. The detectivity D^* ($\text{cm} \cdot \sqrt{\text{Hz}}/\text{W}$) can be found using:

$$D^* = \frac{R_p (A \Delta f)^{1/2}}{i_N} \quad (3)$$

where R_p is the peak absolute response, i_N is the rms noise current, A is the detector area, and Δf is the 1-Hz noise bandwidth. Due to the increased dark current and noise along with a decreased peak responsivity, the D^* of the disordered QWIP is five times lower than that of the as-grown QWIP. With annealing, the rounding of the Al profile results in a reduction of barrier width closest to the continuum, leading to a redshift

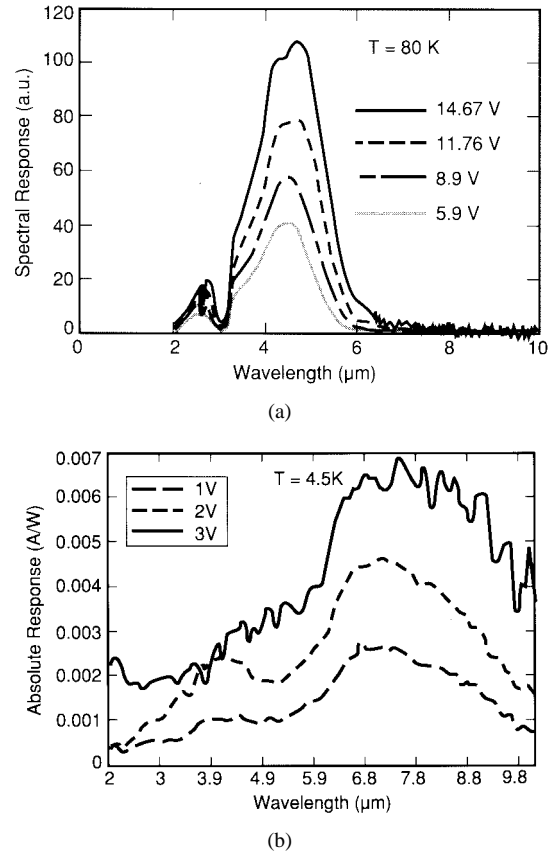


Fig. 17. (a) Bias dependence of the spectral response measured for the as-grown p-type InGaAs–InP QWIP at 80 K. (b) Bias dependence of the spectral response measured for the disordered @ 800 °C for 30 s p-type InGaAs–InP QWIP at 4.5 K.

in the barrier height. As such the thermionic emission current and the thermally assisted tunneling is expected to rise leading to a decrease in detectivity. Redshifting of the intersubband absorption resonance arises both from interdiffusion-induced modification of the confining potential and from a decrease in the depolarization shift. The latter effect is due in part to a decrease in the free-carrier concentration within the Si-doped QW's following rapid thermal annealing [27]. The reduction in electron density by 80% (850 °C RTA) of the as-grown value as observed by the Hall measurements [27], indicates a loss of free carriers in the well for the intersubband transition, attributing substantially to reducing the response and hence the detectivity. But this reduction in detectivity for the GaAs–AlGaAs QWIP may still be acceptable for focal plane array detector applications. Recent advances in growth, complimented by innovative structures (random gratings and reflector layers) should offset any degradation in performance making feasible multiple-colored pixels. Fig. 17(a) and (b) show the photoresponses for both the as-grown and disordered InGaAs/InP detector with bias. The peak response wavelength measured were $\sim 4.55 \mu\text{m}$ (80 K, 5.9 V) for the as-grown detector and $\sim 7.0 \mu\text{m}$ (4.5 K, 4 V) for the disordered (800 °C, 30 s) detector. The peak absolute responses were calculated to be ~ 2.5 A/W (80 K and 5.9 V) for the as-grown detector and ~ 2.0 mA/W (4.5 K and 4 V) for the disordered detector. The peak absolute responsivity of the disordered detector is

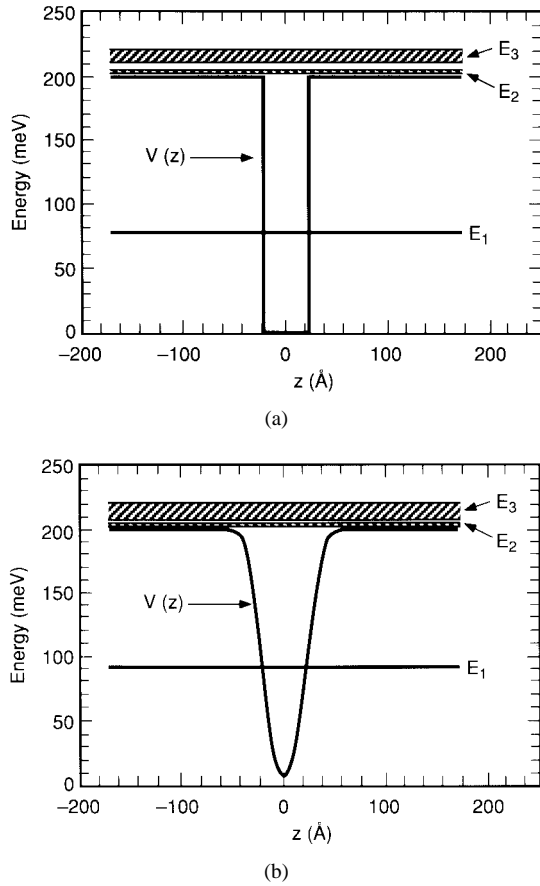


Fig. 18. One period of the MQW structure with its associated energy eigenvalues for the first four subbands for (a) the as-grown QWIP and (b) the disordered QWIP. All widths and compositions are taken from the experimental dates (for n-type GaAs–AlGaAs QWIP).

of a similar magnitude compared to the as-grown detector and the small reduction in the disordered QWIP response is attributed to the out-diffusion of the Be-dopant from the well. For the purpose of our initial comparative study, we have assumed an approx flat optical response in the test temperature regime for InP, as has been verified for GaAs [9]. Further research efforts will attempt extending the temperature ranges and biases. Recent advances in growth, complimented by innovative structures (gratings and reflector layers) should offset any degradation in performance. This makes feasible integration of multiple-colored pixels.

V. COMPARISONS WITH THEORY

The intersubband absorption coefficient spectrum of an MQW or, in general, any periodic or superlattice structure can be derived from Fermi's Golden Rule using the momentum matrix element [36] at

$$\alpha(\omega) = \frac{e^2 \pi}{n_r c \epsilon_0 m_0^2 (\hbar \omega)} \sum_{n,q} |M_{n,q}|^2 \frac{\Gamma}{(E_{n,q} - E_{1,q} - \hbar \omega)^2 + \left(\frac{\Gamma}{2}\right)^2} (N_{1,q} - N_{n,q}) \quad (4)$$

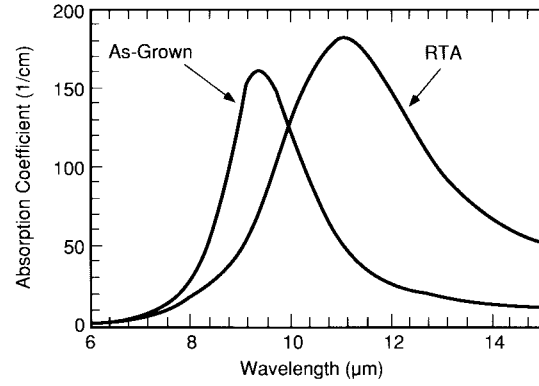


Fig. 19. The calculated absorption coefficient spectra for the as-grown and the disordered n-type GaAs–AlGaAs QWIP. The only fitting parameter used is the linewidth Γ .

where e is the magnitude of the electronic charge, n_r is the refractive index of the material, c is the free-space speed of light, ϵ_0 is the free-space permittivity, m_0 is the free-space electron mass, and $\hbar \omega$ is the energy of a photon. $E_{n,q}$ is the energy eigenvalue of a state with wave vector q in the n th subband of a periodic structure, and $N_{n,q}$ is the volume density of electrons in the state $E_{n,q}$. Γ is the linewidth of the phenomenological linewidth to account for scattering broadening. The momentum matrix element for z -polarized light is given by

$$M_{n,q} = \left\langle \phi_{n,q}(z) \left| \frac{-i\hbar}{m_e^*(z)} \frac{\partial}{\partial z} \right| \phi_{1,q}(z) \right\rangle \quad (5)$$

where $\phi_{n,q}(z)$ is the wave function of the state $E_{n,q}$ and $m_e^*(z)$ is the electron effective mass. The energy eigenvalues and wave functions are found by solving the one-dimensional Schrödinger's equation for an arbitrary periodic potential profile $V(z)$, which is given by

$$-\frac{\hbar^2}{2} \frac{\partial}{\partial z} \left(\frac{1}{m_e^*(z)} \frac{\partial}{\partial z} \phi_{n,q}(z) \right) + V(z) \phi_{n,q}(z) = E_{n,q} \phi_{n,q}(z) \quad (6)$$

In general, the effective mass of an electron $m_e^*(z)$ in an AlGaAs–GaAs MQW structure is a function of the coordinate z . In order to model arbitrary periodic potential profile structures such as as-grown and RTA MQW's, we solve (6) using a Fourier series method [37] to expand each function, such as $\phi_{n,q}(z)$, $V(z)$, and $m_e^*(z)$, into a basis of complex exponentials. Then, the Fourier series coefficients are solved for each energy eigenvalue $E_{n,q}$ to find the wave functions. The wave functions and energy eigenvalues from (6) are used in (4) and (5) to calculate the absorption coefficient of the structure.

To find the potential profile for an RTA MQW structure, it is assumed that the mole fraction of aluminum atoms in one period of an interdiffused MQW structure is given by

$$x(z) = x_B \left\{ 1 - \frac{1}{2} \left[\operatorname{erf} \left(\frac{L_w + z}{2D_{Al}t} \right) + \operatorname{erf} \left(\frac{L_w - z}{2D_{Al}t} \right) \right] \right\} \quad (7)$$

where L_w is the well width, x_B is the mole fraction of aluminum in the barrier before RTA, D_{Al} is the interdiffusion

coefficient of aluminum when using an SiO₂ encapsulant, and t is the anneal time.

The one period of the potential profile and the associated energies of the lowest three subbands are plotted in Fig. 18 for both the as-grown and RTA MQW structures. All values, such as the well and barrier widths and compositions, are taken from the experimental data and growth parameters. An interdiffusion coefficient of $DAI = 4 \text{ \AA}^2/\text{s}$ and a diffusion time of $t = 30 \text{ s}$ is used for the disordered GaAs/AlGaAs structure, which yields a diffusion length of 11 \AA . The value of the interdiffusion coefficient was chosen such that the resulting energy eigenvalues matched the amount of red shift in the intersubband absorption energy measured in Fig. 13. The resulting diffusion length is consistent with the TEM measurement of Fig. 6. In Fig. 19, the absorption coefficient spectra for both as-grown and disordered GaAs–AlGaAs MQW structures are shown. In this case, a broadening parameter Γ was changed from 20 to 30 meV in order to account for the broadened response of the RTA structure, and it is the only fitting parameter used in our model. We note that the peak absorption wavelength and general spectral shapes of the intersubband absorption coefficient agrees well the experimental data shown in Fig. 16.

VI. CONCLUSION

We have demonstrated that impurity-free vacancy disordering can be employed to both shift the operating wavelength and to broaden the response of the GaAs and InP-based QWIP following intermixing of the well and barrier layers during rapid thermal annealing. The intermixing effect on the energy levels is performed based on the Fourier series method and obtain a very good fit. The use of impurity-free vacancy disordering via dielectric encapsulation and rapid thermal annealing changes the well profile of a QWIP and peak wavelength, but the reduced responsivity indicates that this technique is limited for sensitive IR detectors. Recent advances in growth, complimented by innovative structures (random gratings and reflector layers) should offset any degradation in performance. This makes feasible integration of multiple-colored/broad spectrum pixels.

ACKNOWLEDGMENT

The authors would like to thank Profs. N. Holonyak Jr., S. G. Bishop, I. Adesida, N. F. Gardner, A. P. Curtis and H. C. Kuo of the University of Illinois at Urbana-Champaign, Dr. H. C. Liu of National Research Council, Canada, Dr. K. K. Choi of U.S. Army Research Laboratory, NJ, Dr. M. Dodd and Dr. J. Scheihing of WPAFB, OH, and Prof. E. H. Li of the University of Hong Kong for many helpful discussions. They would also like to acknowledge D. Cuda (JPL) for the help with the manuscript preparation.

REFERENCES

- [1] A. Rogalaki, "Selected papers on semiconductor infrared detectors," *SPIE Milestone Series*, B. J. Thompson, Series Editor. Bellingham, WA: SPIE, vol. MS66, 1992.
- [2] P. R. Norton, "Infrared image sensors," *Opt. Eng.*, vol. 30, p. 1649, 1991.
- [3] R. B. Emmons, SR. Hawkins, and K. F. Cuff, "Infrared detector: An overview," *Opt. Eng.*, vol. 14, p. 21, 1975.
- [4] L. Esaki, G. A. Sai-Halasz, and L. L. Chang, "Infrared optical devices of layered structure," U.S. Patent 4 205 331, May 27, 1980.
- [5] J. S. Smith, L. C. Chiu, S. Margaht, A. Yariv, and A. Y. Cho, "A new infrared detector using electron emission from multiple quantum wells," *J. Vac. Sci. Technol. B.*, vol. 1, p. 376, 1983.
- [6] O. Byung-sung, J. W. Choe, M. H. Francombe, K. M. S. V. Bandara, D. D. Coon, Y. F. Lin, and W. J. Takei, "Long wavelength infrared detection in a kastalsky-type superlattice structure," *Appl. Phys. Lett.*, vol. 57, p. 503, 1990.
- [7] M. A. Kinch and A. Yariv, "Performance limitations of GaAs/AlGaAs infrared superlattice," *Appl. Phys. Lett.*, vol. 55, p. 2093, 1989.
- [8] B. F. Levine, K. K. Choi, C. G. Bether, J. Walker, and R. J. Malik, "New $10 \mu\text{m}$ infrared detector wing intersubband absorption in resonant tunneling GaAlAs superlattices," *Appl. Phys. Lett.*, vol. 50, p. 1092, 1987.
- [9] B. F. Levine, "Quantum-well infrared photo-detectors," *J. Appl. Phys.*, vol. 74, p. R1, 1993.
- [10] S. A. Lyon, "Long wavelength quantum well detectors: Can they compete," *Surf. Sci.*, vol. 228, p. 508, 1990.
- [11] S. D. Gunapala, J. S. Park, G. Sarusi, T. L. Lin, J. K. Liu, P. D. Maker, R. E. Muller, C. A. Shott, and T. Hoelter, " $15 \mu\text{m}$ 128×128 GaAs/Al_xGa_{1-x}As quantum well infrared photodetector focal plane array camera," *IEEE Trans. Electron Devices*, vol. 44, pp. 45–50, Jan. 1997.
- [12] M. G. Moharam and T. K. Gaylord, "Diffraction analysis of surface-relief gratings," *J. Opt. Soc. Amer.*, vol. 72, p. 1385, 1982.
- [13] G. Hasnaian, B. F. Levine, C. G. Bethea, R. A. Logan, J. Walker, and R. T. Malik, "GaAs/AlGaAs multiquantum well infrared detector arrays using etched gratings," *Appl. Phys. Lett.*, vol. 54, p. 5215, 1989.
- [14] J. Katz, Y. Zhang, and W. P. Wang, "Normal incidence infrared absorption in AlAs/AlGaAs x-valley multiquantum wells," *Appl. Phys. Lett.*, vol. 61, p. 1697, 1992.
- [15] J. Y. Anderson and L. Lundquist, "Near-unity quantum efficiency of AlGaAs/GaAs quantum well infrared detector, using a waveguide with a doubly periodic grating coupler," *Appl. Phys. Lett.*, vol. 59, p. 857, 1991.
- [16] G. Sarusi, B. F. Levine, S. J. Pearton, K. M. S. Bandara, and R. E. Lebeguth, "Optimization of two dimensional gratings for very wavelength QWIP," *J. Appl. Phys.*, vol. 76, p. 4989, 1996.
- [17] V. Jandhyala, E. Michielssen, B. Shanker, and W. Chew, Center for Computational Electromagnetics, Univ. of Illinois, Urbana, Tech. Rep. CEM-3-97, 1997.
- [18] V. Jandhyala, D. K. Sengupta, B. Shanker, E. Michielssen, M. Feng, and G. E. Stillman, "Efficient electromagnetic analysis of two-dimensional finite quasirandom gratings for quantum well infrared photodetectors," *J. Appl. Phys.*, vol. 83, no. 6, p. 3360, 1998.
- [19] M. B. Stern and S. S. Medeiros, "Deep three dimensional microstructure fabrication for infrared binary optics," *J. Vac. Sci. Technol. B.*, vol. 10, pp. 2520–2525, 1992.
- [20] K. K. Choi, M. Z. Tidrow, M. Taysing-Lam, W. H. Chang, C. H. Kuan, C. W. Farles, and F. Chong, "Low dark current infrared hot-electron transistor for 77 K operation," *Appl. Phys. Lett.*, vol. 63, p. 908, 1993.
- [21] K. L. Tsai, K. H. Chang, C. P. Lee, K. F. Huang, J. S. Tsang, and H. R. Chen, "Two-color infrared photodetector using GaAs/AlGaAs and strained InGaAs/AlGaAs multiquantum wells," *Appl. Phys. Lett.*, vol. 62, pp. 3504, 1993.
- [22] M. Z. Tidrow, K. K. Choi, A. J. DeAnni, and W. H. Chang, "Grating coupled multicolor quantum well infrared photodetectors," *Appl. Phys. Lett.*, vol. 67, p. 1800, 1995.
- [23] W. D. Laidig, N. Holonyak, Jr., M. D. Camras, K. Hess, J. J. Coleman, P. D. Dapkus, and J. Bardeen, "Disorder of an AlAs-GaAs superlattice by impurity diffusion," *Appl. Phys. Lett.*, vol. 38, p. 776, 1981.
- [24] J. H. Marsh and A. C. Bryce, "Fabrication of photonic integrated circuits using quantum well intermixing," *Mater. Sci. Eng. B.*, vol. 24, p. 272, 1994.
- [25] J. J. Coleman, P. D. Dapkus, C. G. Kirkpatrick, M. D. Camras, and N. Holonyak, "Disorder of an AlAs GaAs superlattice by silicon implantation," *Appl. Phys. Lett.*, vol. 40, p. 904, 1982.
- [26] H. H. Tan, J. S. Williams, C. Jagadish, P. T. Burke, and M. Gal, "Large energy shifts in GaAs–AlGaAs quantum wells by proton irradiation induced intermixing," *Appl. Phys. Lett.*, vol. 68, p. 2401, 1996.
- [27] J. D. Ralston, M. Ramsterner, B. Dischler, M. Maier, P. Koidl, and D. J. As, "Intersubband transitions in partially interdiffused GaAs/AlGaAs multiple quantum well structures," *J. Appl. Phys.*, vol. 70, p. 2195, 1991.

- [28] A. G. Steele, M. Buchanan, H. C. Liu, and Z. R. Wasliewski, "Post-growth tuning of quantum well infrared detectors by rapid thermal annealing," *J. Appl. Phys.*, vol. 75, p. 8234, 1994.
- [29] E. H. Li, "Diffused quantum well structures: Advances in materials & device realization," *Mat. Res. Soc. Symp. Proc.*, vol. 450, 1997.
- [30] B. S. Ooi, C. J. Hamilton, K. McIlvaney, A. C. Bryce, R. M. De La Rue, J. H. Marsh, and J. S. Roberts, "Quantum-Well intermixing in GaAs-AlGaAs structures using pulsed laser irradiation," *IEEE Photonics Letters*, vol. 9, no. 5, May 1997.
- [31] D. K. Sengupta, T. Horton, W. Fang, A. Curtis, J. Li, S. L. Chuang, M. Feng, G. E. Stillman, A. Kar, J. Mazumder, L. Li, and H. C. Liu, "Red-shifting of a bound-to-continuum GaAs/AlGaAs quantum well infrared photodetector response via laser annealing," *Appl. Phys. Lett.*, vol. 70, p. 3573, 1997.
- [32] C. J. McLean, A. McKee, G. Lullo, A. C. Bryce, R. M. De La Rue, and J. H. Marsh, "Quantum well intermixing with high spatial selectivity using a pulsed laser technique," *Electron. Lett.*, vol. 31, p. 1285, 1995.
- [33] T. K. Sudoh, M. Kumano, Y. Nakano, and K. Tada, "Wavelength trimming by photoabsorption induced disordering for multiple wavelength distributed feedback laser arrays," *IEEE Photon. Technol. Lett.*, vol. 9, pp. 887-888, July 1997.
- [34] M. K. Kelley, J. Rogg, C. E. Nebel, M. Stutzmann, and S. Katai, "High resolution thermal processing of semiconductor using pulsed-laser interference patterning," *Phys. Status Sol. (a)*, vol. 166, p. 651, 1998.
- [35] D. Bauerle, "Laser-induced fabrication and processing of semiconductors: Recent developments," *Phys. Status Sol. (a)*, vol. 166, p. 543, 1998.
- [36] S. L. Chuang, *Physics of Optoelectronic Devices*. New York: Wiley, 1995.
- [37] K. T. Kim, S. S. Lee, and S. L. Chuang, "Inter-miniband optical absorption in a modulation-doped $\text{Al}_x\text{Ga}_{1-x}\text{As}/\text{GaAs}$ superlattice," *J. Appl. Phys.*, vol. 69, p. 6617, 1991.
- Peter Apostolakis**, photograph and biography not available at the time of publication.
- Kwong-Chi Hseih**, photograph and biography not available at the time of publication.
- Yia-Chung Chang**, photograph and biography not available at the time of publication.
- Shun Lien Chuang**, photograph and biography not available at the time of publication.
- Sumith Bandara**, photograph and biography not available at the time of publication.
- Deepak Sengupta**, photograph and biography not available at the time of publication.
- Sarath Gunapala**, photograph and biography not available at the time of publication.
- Vikram Jandhyala**, photograph and biography not available at the time of publication.
- Milton Feng**, photograph and biography not available at the time of publication.
- Sangsig Kim**, photograph and biography not available at the time of publication.
- Eric Michielssen**, photograph and biography not available at the time of publication.
- Weich Fang**, photograph and biography not available at the time of publication.
- Greg Stillman**, photograph and biography not available at the time of publication.
- Jay Malin**, photograph and biography not available at the time of publication.